To be published in the Proceedings of the 1996 National Thermal Spray Conference (NTSC'96), Cincinnati, Ohio, Oct. 7-11, 1996 -- available from ASM International, Materials Park, OH 44073

Computational Fluid Dynamics Analysis of a Wire-Feed, High-Velocity Oxygen-Fuel (HVOF) Thermal Spray Torch*

Amalia R. Lopez, Basil Hassan, William L. Oberkampf, Richard A. Neiser, and Timothy J. Roemer

Sandia National Laboratories

Albuquerque, New Mexico

Abstract

The fluid and particle dynamics of a High-Velocity Oxygen-Fuel Thermal Spray torch are analyzed using computational and experimental techniques. Three-dimensional Computational Fluid Dynamics (CFD) results are presented for a curved aircap used for coating interior surfaces such as engine cylinder bores. The device analyzed is similar to the Metco Diamond Jet Rotating Wire (DJRW) torch. The feed gases are injected through an axisymmetric nozzle into the curved aircap. Premixed propylene and oxygen are introduced from an annulus in the nozzle, while cooling air is injected between the nozzle and the interior wall of the aircap. The combustion process is modeled using a single-step finite-rate chemistry model with a total of 9 gas species which includes dissociation of combustion products. A continually-fed steel wire passes through the center of the nozzle and melting occurs at a conical tip near the exit of the aircap. Wire melting is simulated computationally by injecting liquid steel particles into the flow field near the tip of the wire. Experimental particle velocity measurements during wire feed were also taken using a Laser Two-Focus (L2F) velocimeter system. Flow fields inside and outside the aircap are presented and particle velocity predictions are compared with experimental measurements outside of the aircap.

HIGH-VELOCITY OXYGEN-FUEL (HVOF) THERMAL SPRAYING uses a combustion process to heat the gas flow and coating material. The two-phase gas and particle flow is then accelerated to high velocities outside of the torch. HVOF torches normally produce temperatures around 3000 *K*; whereas, in plasma spraying, it is typically around 10,000 *K*. A lower temperature range causes the gas density in HVOF torches to be higher than in plasma torches. The combination of high gas density and high gas velocity tends to produce higher density coatings.

* This work was performed at Sandia National Laboratories, which is operated by Lockheed Martin for the U. S. Department of Energy under Contract DE-AC04-94AL85000.

Because of recent advances in CFD methods and computer power, CFD codes can now be used to simulate the HVOF spraying process. The first CFD simulation of the HVOF process was conducted by Power et al.[1,2] and Smith et al.[3] They performed an axisymmetric analysis of the internal flow and external flow of the Metco Diamond Jet torch with a powder feeder. For the internal flow, a two-step finite-rate chemistry model was used to model the combustion of propylene (C_3H_6). For the external flow, they assumed that the flow at the exit had reached chemical equilibrium so they did not model any chemical kinetics. Inside the aircap, they injected tracker particles of various sizes. These particles were affected by the local gas velocity and temperature, but they did not have any effect on the gas stream.

Oberkampf and Talpallikar[4,5] also analyzed the fluid and particle dynamics of a similar axisymmetric geometry. They modeled the HVOF process with full coupling between the interior and exterior flow fields. A one-equation, approximate equilibrium chemistry model was used to model the combustion of propylene. An Eulerian/Lagrangian approach was used to model the gas and solid phases, respectively. The gas and particles were fully coupled through momentum and energy exchanges.

Hassan, et al.[6] analyzed the gas flow field of an axisymmetric thermal spray device. They also modeled the HVOF process with full coupling between the interior and exterior flow fields. Both a single-step and a 12-step quasi-global finite-rate chemistry model were used to model the combustion of propylene. The CFD results compared well with experimental measurements of pressure inside the HVOF aircap for supersonic flow, but somewhat underpredicted the pressure for subsonic flow. In their analyses, it was found that the single-step chemistry model compared very well with the 12-step chemistry model and was shown to be applicable for predicting thermal spray combustion chemistry.

Hassan, Lopez, and Oberkampf[7] performed the first three-dimensional analysis of a thermal spray device. They simulated the gas flow in the aircap and external to the aircap with full coupling between the interior and exterior flow fields. An approximate equilibrium chemistry model was used to model the combustion process. Gas flow fields both

DISCLAIMER

inside and outside the aircap were presented and discussed.

The present work will show the first CFD calculations made on a three-dimensional aircap with wire feed. The aircap geometry is similar to the Metco DJRW torch. A solid model representation of this aircap is shown in Fig. 1. This paper describes the general gas dynamic features of the complex, three-dimensional flow field as well as the particle dynamic features of the metal particles. An Eulerian-Lagrangian technique is used to couple the fluid dynamics of the gas flow to that of the particles. The gas temperature, Mach number distributions, and streamline patterns are predicted inside and outside the torch. Experimental particle velocity measurements were also taken using a Laser Two-Focus (L2F) velocimeter system. Particle velocity measurements were obtained in the plane of symmetry of the aircap and compared with the CFD predictions.

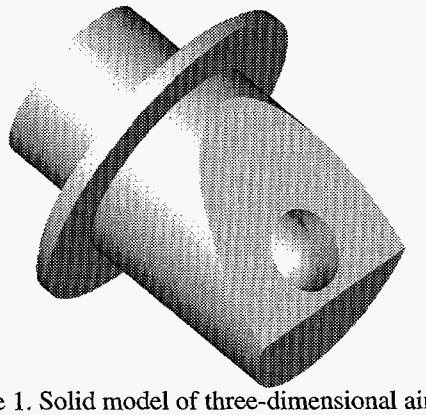

Figure 1. Solid model of three-dimensional aircap.

Gas Dynamics Modeling

The numerical simulations are made using a commercial CFD code, CFD-ACE.[8,9] CFD-ACE is a pressure-based code that solves the three-dimensional, Favre-averaged Navier-Stokes equations. These equations model the conservation of mass, momentum, and energy for unsteady, compressible, turbulent flows. The governing equations are solved sequentially in an implicit, iterative manner using a finite volume formulation. Various options for modeling turbulence, reaction chemistry, and multi-phase flows are available in this code. In the present calculations, the governing equations are solved until a steady-state solution is reached. The k-ε turbulence model of Launder and Spaulding[10] is used along with the compressibility correction of Sarkar.[11] For further details on the numerical algorithms, see Refs. 8-9.

Chemistry Modeling

The number of intermediate gas species and reactions used in hydrocarbon-oxygen reaction models vary greatly, depending on the model requirements. Given that computer time is greatly increased with the solution of multiple-step chemistry models, the present approach uses a single-step finite-rate chemistry model to represent the hydrocarbon combustion process inside the aircap. Hassan, et al.[6] found that equilibrium chemistry, and its approximations, produced numerical solutions whose energy release was dependent on spatial grid size. They determined that as the grid spacing in the chemical reaction cell was reduced, the heat release was confined to a smaller region which resulted in a very high, unrealistic, inlet pressure. Therefore, it was necessary to use a chemistry model which spreads out the heat release over some distance, just as it occurs physically. While a 12-step chemistry model includes more intermediate reactions, Hassan, et al.[6] determined that a single-step chemistry model adequately represented the combustion of propylene. In the present analysis, a fully-mixed fuel and oxygen stream was also assumed in order to begin the simulation inside the aircap. The validity of this assumption, however, is difficult to determine.

The single-step reaction was derived from the One-Dimensional Equilibrium Chemistry code developed by Gordon and McBride[12] and is of the form:

$$C_3H_6 + x\,O_2 \Rightarrow Products$$

where x is the number of moles of oxygen that react with one mole of propylene. The products of combustion included CO_2, H_2O, CO, H_2, OH, H, and O. Nitrogen (N_2) was assumed inert at the temperatures considered. Given a specified fuel-oxygen mixture ratio, pressure, and temperature (those of the premixed fuel and oxygen stream), the One-Dimensional Equilibrium Chemistry code[12] determined the equilibrium composition that is shown by the following balanced reaction:

$$\begin{aligned} C_3H_6 + 3.6646\,O_2 \Rightarrow\ & 1.0924\,CO_2 + 1.9076\,CO \\ & + 1.9432\,H_2O + 0.8215\,OH \\ & + 0.4329\,H_2 + 0.4263\,H + 0.4721\,O \end{aligned}$$

The reaction rate, k_f, used in this investigation is from the work of Westbrook and Dryer[13] and is defined as follows:

$$k_f = AT^{\eta}\exp(E_a/(RT))[C_3H_6]^a[O_2]^b$$

where T is the local gas temperature, E_a is the activation energy, and A, η, R, a, and b are constants. The reaction constants given by Westbrook and Dryer[13] were originally calibrated for laminar diffusion flames at different flow conditions. Therefore, some adjustments in these constants were necessary to model turbulent flames. For example, the pre-exponential factor, A, was adjusted in order to match the experimentally observed flame length inside the thermal spray torch. The value of A and all of the reaction constants used were the same as given by Hassan, et al.[6]

Liquid Particle Modeling

The liquid droplet equations are solved in a Lagrangian frame of reference moving with the particles. The solutions to these equations are used to calculate the source/sink terms for the corresponding gas phase equations which are solved in an Eulerian frame of reference. The dominant coupling between the particle and gas phases is due to momentum transfer; energy coupling is secondary. The equation of motion for the particle is written as:[14]

$$m_p\frac{dU_p}{dt} = \frac{1}{2}\rho A_p C_d(U-U_p)|U-U_p| - V_p\nabla p + m_p g$$

where m_p is the mass of the particle and U_p is the velocity vector of the particle. C_D is the drag coefficient, and ρ, U, and p are the density, velocity, and pressure of the gas, respectively. A_p is the particle surface area and V_p is the particle volume. The gravity vector is represented by g. The liquid particles are assumed to be spherical during their entire trajectory. The equation of motion for a particle accounts for the acceleration/deceleration of the particle due to the combined effects of drag from the gas flow, local pressure gradients of the gas, and body forces such as gravity.

The drag coefficient for the particle is a function of the local Reynolds number of the particle which is evaluated as:

$$Re = \frac{\rho|U - U_p|d_p}{\mu}$$

where d_p is particle diameter and μ is the molecular viscosity of the local gas mixture. The following correlations have been found to be valid for a wide range of Reynolds numbers[14]

$$C_d = \frac{24}{Re} \qquad \text{for } Re < 1$$

$$C_d = \frac{24}{Re}(1 + 0.15Re^{0.67}) \qquad \text{for } 1 < Re < 10^3$$

$$C_d = 0.44 \qquad \text{for } Re > 10^3$$

These drag coefficient relations have been shown to be reliable for particle Mach numbers less than unity, relative to the local gas speed of sound. The relative Mach number of the particle is given by

$$M_p = \frac{|U - U_p|}{\sqrt{\gamma RT}}$$

where γ is the ratio of specific heats of the gas, R is the gas constant, and T is the gas temperature. γ, R, and T are all evaluated at the particle location and are dependent on the local mixture of gas species.

Aircap Geometry and Grid Generation

The geometry of the aircap is similar to a Metco DJRW torch. Figure 2 shows a computational grid in the plane of symmetry of the curved aircap. The interior of the aircap is composed of a converging conical section and two cylindrical sections that are blended together by a portion of a sphere. The turn angle between the two cylinder centerlines is 60 degrees. There are two sets of inlet streams: the premixed fuel and oxygen stream, and the annular air cooling stream along the surface of the aircap. In the Metco hardware, the fuel-oxygen stream is fed into the aircap by ten equally spaced holes around the nozzle just inside the circumferential lip of the nozzle. In the present analysis, the fuel-oxygen inlet is modeled as an annulus that has the same total area as the ten holes and is centered at the same radial location as the holes in the nozzle. This assumption greatly simplifies the numerical analysis by reducing the size of the aircap grid in the circumferential direction.

Figure 2 also shows a steel wire positioned in the aircap. The centerlines of the nozzle and the metal wire have been shifted vertically upward by 0.406 *mm* (0.016 *in*) from the centerline of the conical portion of the aircap. This shift is necessary to provide more air cooling flow to the bottom portion of the aircap where the highest heat transfer rates would occur without an offset. Both the premixed fuel-oxygen and the air cooling streams are angled 5 degrees to the centerline of the nozzle.

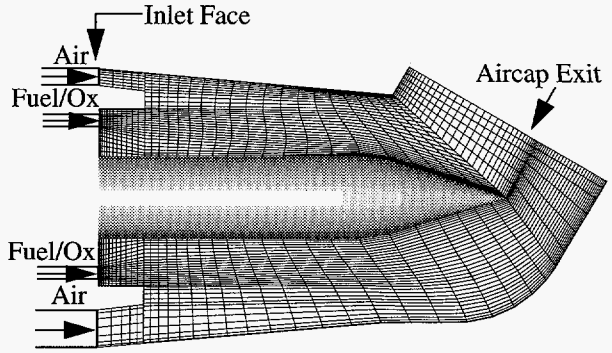

Figure 2. Interior aircap grid in plane of symmetry (every other grid line shown).

At the inlet face of the torch in Fig. 2, the inner radius of the aircap is 5.59 *mm* (0.22 *in*) and the outer radius of the nozzle is 4.13 *mm* (0.1625 *in*). The outer radius of the fuel-oxygen annulus is 3.10 *mm* (0.1222 *in*) and the inner radius is 2.79 *mm* (0.1098 *in*). The radius of the metal wire is 1.59 *mm* (0.0625 *in*), and the aircap exit radius is 4.41 *mm* (0.1735 *in*).

GRIDGEN[15] Version 10 was used to generate the computational grid used in the CFD calculations. The interior grid shown in Fig. 2 was created in three blocks: the air inlet section, the fuel-oxygen inlet section, and the remaining aircap section up to the exit. Because of symmetry about the centerline plane, only half of the aircap was simulated. Figure 2 shows the radial grid clustering that was used to resolve the shear layers surrounding the fuel-oxygen inlets, the edge of the flame, and the boundary layers along the surface of the aircap and the wire. In the axial direction, the grid was clustering at the fuel-oxygen inlet and then gradually stretched towards the exit of the aircap. Axial clustering was necessary to numerically stabilize the combustion process and accurately model the large energy release in the computational cells of the reaction zone. The grid was also clustered on the leeside of the conical tip to capture the wake flow off of the wire. The number of grid points in the interior of the aircap are 26 (axial) by 41 (radial) by 20 (circumferential) in the fuel-oxygen inlet section, 12 (axial) by 16 (radial) by 20 (circumferential) in the air inlet section, and 56 (axial) by 65 (radial) by 20 (circumferential) in the remaining aircap section.

Figure 3 shows the exterior grid in the plane of symmetry outside of the aircap. The upper and lower boundaries extend 13 aircap exit radii from the centerline and the outlet boundary extends 14 aircap exit radii from the aircap exit. For simplicity of boundary conditions, a solid circular wall was assumed in the exit plane of the aircap. Grid points were highly clustered in the jet decay region outside the torch as shown by the solid black region in Fig. 3. In addition, the ex-

terior grid lines were tilted downward from the geometric centerline of the aircap exit plane to better align the grid with the expected jet flow direction. The number of grid points in the exterior of the aircap are 71 (axial) by 86 (radial) by 20 (circumferential). The total number of grid points (in the half-volume), interior and exterior to the aircap, for this three-dimensional calculation was 220,080.

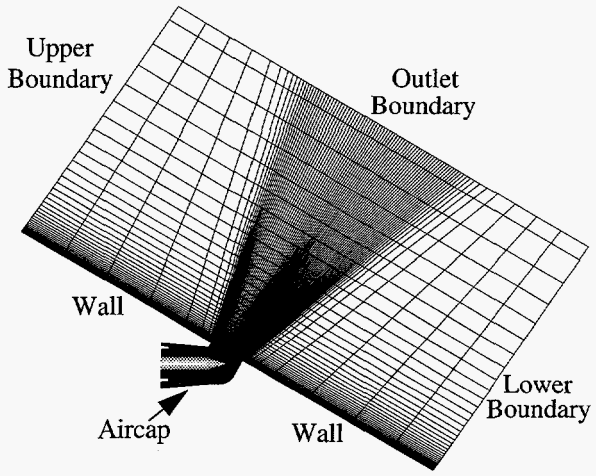

Figure 3. Exterior grid in plane of symmetry (every other grid line shown).

Boundary Conditions

Table 1 lists the mass flow rates and gas temperatures that were specified at each inlet in the present simulation. All of the interior walls of the aircap, nozzle, and wire surface are modeled with a no-slip, fixed temperature condition. The wall temperature on all surfaces of the nozzle were specified to be 850 *K*. The wall temperature of the aircap was assumed to be 305 *K*. It was also necessary to assume the turbulent length scales of the inlet streams based on the physical size of the inlets, and a 10% turbulence intensity. To determine the actual turbulent values would require modeling the flow in the fuel, oxygen, and air feeder tubes. The turbulent values used in the simulation are given in Table 2.

Table 1. Mass Flow Rates and Inlet Temperatures

Gas	Mass Flow Rates		Temperature
	SCFH	*(kg/sec)*	*(K)*
Propylene	100.0	1.350×10^{-3}	450.0
Oxygen	450.0	4.630×10^{-3}	450.0
Air	1100.0	1.024×10^{-2}	330.0

In the actual Metco device, wire is continually fed at a constant rate such that the wire tip remains fixed relative to the aircap. This allows the wire to be modeled as a fixed no-slip wall. A linear temperature distribution is specified along the wire that varies from 330 *K* at the inlet to 1780 *K* at the shoulder of the wire, i.e., at the beginning of the wire tip. Since the steel wire is melting along the tip, a constant value of 1780 *K* was assumed on the conical tip. The value at the inlet was chosen to be slightly higher than ambient temperature due to heat conduction through the nozzle. The value at the conical tip is the melting temperature of steel.

Table 2. Turbulent Kinetic Energy and Dissipation

Inlet	Turbulent Kinetic Energy ($k=m^2/s^2$)	Dissipation Rate ($\varepsilon=m^2/s^3$)
Fuel/Ox	2600	9.840×10^{8}
Air	120	2.920×10^{6}

In the present analysis, it is assumed that the HVOF torch exhausts into ambient air at a temperature of 303 *K* and a pressure of 83427 *Pa*, atmospheric pressure for Albuquerque, New Mexico where the experimental data were taken. In the exterior grid, the boundary surrounding the aircap exit is specified to be a fixed temperature, no-slip wall, the upper and lower outer boundary is specified to be a fixed pressure inlet/outlet, and the outlet boundary is specified to be a zero-pressure gradient outlet. In the plane of symmetry, a symmetry condition is specified for both the interior and exterior domains.

In the Metco device, a liquid layer of steel forms along the conical tip as the wire melts. The droplets are then stripped off the actual tip of the wire by the surface shear stress of the gas acting on the liquid layer. In the present simulation, the stripping of the liquid droplets from the wire tip is modeled as ten steel particles injected along the leeside of the conical tip near the plane of symmetry. The small number of computational particles as compared to the number of physical particles is not critically important for adequate simulations. The important parameter to match in the simulation is the mass flow rate of the particles. The particle size is 30 μm, the temperature is 1900 *K*, and the velocity is zero for initial conditions at each injection point. The particle size was based on Phase Doppler Particle Analyzer (PDPA) measurements in previous experiments which produced a number geometric mean diameter of approximately 30 μm. Note that this experimental measurement was outside the aircap, after droplet break-up was complete. The initial particle temperature was chosen to be 120 degrees higher than the melt temperature because it is assumed that some particle superheating occurs in flight; however, the numerical results were not sensitive to particle temperature. The mass loading is based on a 40 *in/min* wire feedrate which results in a 1.054×10^{-3} *kg/sec* mass flow rate of the particles.

Computational Requirements

The computational simulations were converged 4-5 orders of magnitude reduction in all residuals over the computational domain. Typically, 3000 iterations were required to obtain 4-5 orders of magnitude reduction in the residuals. These solutions require multiple restarts to improve input parameters and grid quality. The solution required 3.0 *msec/cell/iteration* of CPU time and 250 *Mbytes* of RAM on a Sun Microsystems SPARCstation 10 Model HS125 workstation. These 3000 iterations required a total CPU time of 500 hours.

Experimental Measurements

The experimental data were taken in the Thermal Spray Research Laboratory at Sandia National Laboratories. Gas flows to the Metco DJRW torch were set using a Metco ATC controller. The ATC uses Hasting-Teledyne 200 Series mass-flow controllers to meter the gas flow rates. The gas flows used in this experiment are given in Table 1. The wire feed rate was approximately 21 *mm/sec* (50 *in/min*).

Particle velocity distributions were measured in the HVOF jet using a Laser Two-Focus (L2F) velocimeter. A detailed description of this device has been published previously.[16] The 30 micron particle size used in the simulations was based on Phase Doppler Particle Analyzer (PDPA) measurements made using similar, but not identical, torch geometries and gas flow rates. However, it has been shown that particle size distributions are relatively insensitive to these process variations.[17] In the simulations presented in this paper, discrete particles of a fixed size are released at various locations in the vicinity of the wire tip. In reality, the wire melting and droplet atomization process produces a particle stream that has size and velocity distributions that vary as a function of position in the jet.[17] A 30 micron size was selected because it is the number geometric mean size of particle size distributions measured several centimeters downstream of the wire tip when atomization is complete. That is, it is the most frequently produced particle size in the plume.

At each point in the plume a particle velocity distribution was measured using the L2F. The velocity distributions had a slowly falling high velocity tail associated with finely atomized particles.[17] A single particle velocity needed to be extracted from each velocity distribution for comparison with calculated values. PDPA measurements of particle size-velocity correlations revealed that, for at least the first 5 *cm* downstream of the wire tip, particle size is essentially independent of particle velocity.[17] For this reason, the mode of the particle velocity distribution (i.e., the most frequently recorded velocity) rather than the mean of the distribution was used. The velocity mode was typically about 5% slower than the velocity mean at any given point in the plume.

Experimental measurements of particle velocity were made along a 2-D grid oriented at a 45 degree angle with respect to the wire axis. The origin of the grid was at the center of the exit hole in the curved aircap. Measurements were made axially along the jet in 1 *cm* increments out to 10 *cm* and radially in 0.2 *cm* increments over the range +/- 0.4 *cm*. The center of the particle jet followed a trajectory tilted at ~6 degrees with respect to the grid's axial direction. Consequently, some measurements of the densest part of the particle plume at axial distances greater than ~4 *cm* were not made.

Results

Internal Flow Field. The computed gas temperature contours in the plane of symmetry of the aircap are shown in Fig. 4. The inflow of the premixed fuel-oxygen stream can be seen as the low temperature (dark) regions above and below the wire. Combustion occurs primarily on the inner and outer mixing layers of the annular injection of the premixed fuel and oxygen. The flame is approximately 7 *mm* long and the peak temperature in the flow field is 3330 *K*. Along the top and bottom surface of the aircap, an annular jet of air is injected between the nozzle and the aircap. The air layer on the bottom of the aircap is thicker due to the vertical shift between the nozzle and the aircap. This shift is necessary to keep the bottom curved portion of the aircap from melting. Simulating the gas flow through the aircap with wire feed also produces a wake region above the leeside of the wire tip. In the wake region, the temperature of the gas is reduced approximately 500 *K* from the surrounding combustion gas temperatures.

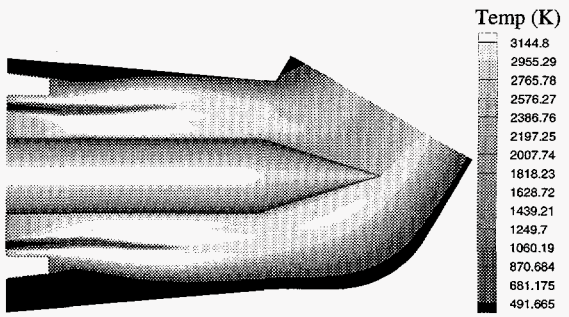

Figure 4. Plane of symmetry gas temperature contours inside aircap.

Figure 5 shows the streamline pattern in the plane of symmetry of the aircap. A large recirculation flow region can be seen between the wire and the fuel-oxygen jet and a small region can also be seen above the jet. These high temperature combustion products are trapped in a vortical flow which continually ignites the incoming fuel-oxygen stream. A small recirculation region is also seen in the base flow region of the nozzle lip between the fuel-oxygen inlet and the air inlet. On the upper surface of the aircap, near the exit, the boundary layer separates from the wall as the flow tries to turn the sharp corner. The streamline pattern shows that flow from the ambient exterior region is sucked into the aircap in the separated region. Finally, this figure shows that along the cylindrical portion of the wire the flow is essentially axial, but along the conical tip, crossflow over the tip occurs due to the aircap turning the stream. Sufficient crossflow is generated so that a small separated flow region is formed on the leeside of the wire.

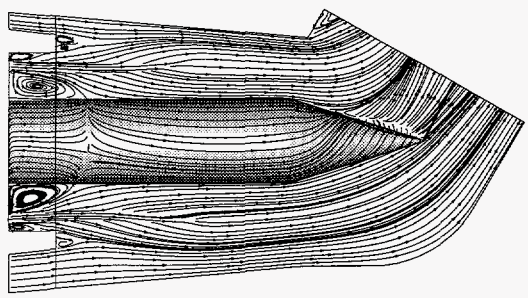

Figure 5. Plane of symmetry and wire surface streamline pattern inside aircap.

Figure 6 shows gas Mach number contours in the circular exit plane of the aircap, i.e., normal to the view in previous figures. At the top of the aircap exit, there is a subsonic flow region where the air from the ambient is flowing into the aircap. Between this separated flow region and the middle of the aircap exit, the flow is supersonic. In lower half of the aircap exit, which is mostly subsonic, there is a spoon-shaped region of lower speed flow that is caused by the wake flow off the wire. This figure clearly shows the complex 3-D flow exiting this type of thermal spray torch. There is a range in Mach numbers from low subsonic, where there is flow into the torch, to a peak Mach number of 1.75.

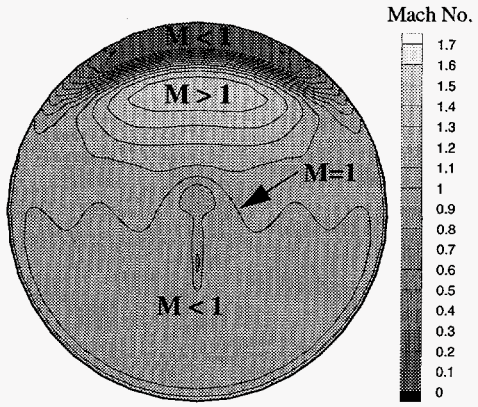

Figure 6. Gas Mach number contours in the exit plane of the aircap.

External Flow Field. Gas Mach number contours in the plane of symmetry are shown in Fig. 7. The peak Mach number in the supersonic jet occurs within one exit diameter from the aircap and has a value of 2.5. The peak Mach number occurs exterior to the torch because the aircap operates as an underexpanded nozzle, i.e., the flow expands to match the ambient pressure outside of the aircap. Recall that the Mach number is the ratio of the local gas speed to the local speed of sound. Because of the high gas temperatures in the jet, the local speed of sound at the peak Mach number is about 1200 *m/sec*.

At the exit of the aircap, the flow expands to ambient pressure through a series of expansion and compression waves known as shock diamonds. The first series of waves exterior to the aircap are expansion waves. These waves reflect from the free jet boundaries as compression waves, resulting in the first shock diamond about 1.5 exit diameters from the exit. Only one distinct shock diamond can be seen in the flow field, the dark region of lower Mach number. Increased grid resolution in this region would pick up other diamonds, as seen experimentally. The strength of the expansion and compression waves decreases as the flow convects downstream and the supersonic core flow is dissipated as it mixes with the ambient air. The supersonic region, however, extends to the end of the calculation domain.

Streamline patterns overlaid on pressure contours in the plane of symmetry are shown in Fig. 8. The streamline pattern clearly shows the jet flow from the aircap exit to the end of the computational domain. It can be seen that the jet is not aligned normal to the exit plane of the aircap. The jet has been directed downward by the separated shear layer that ex-

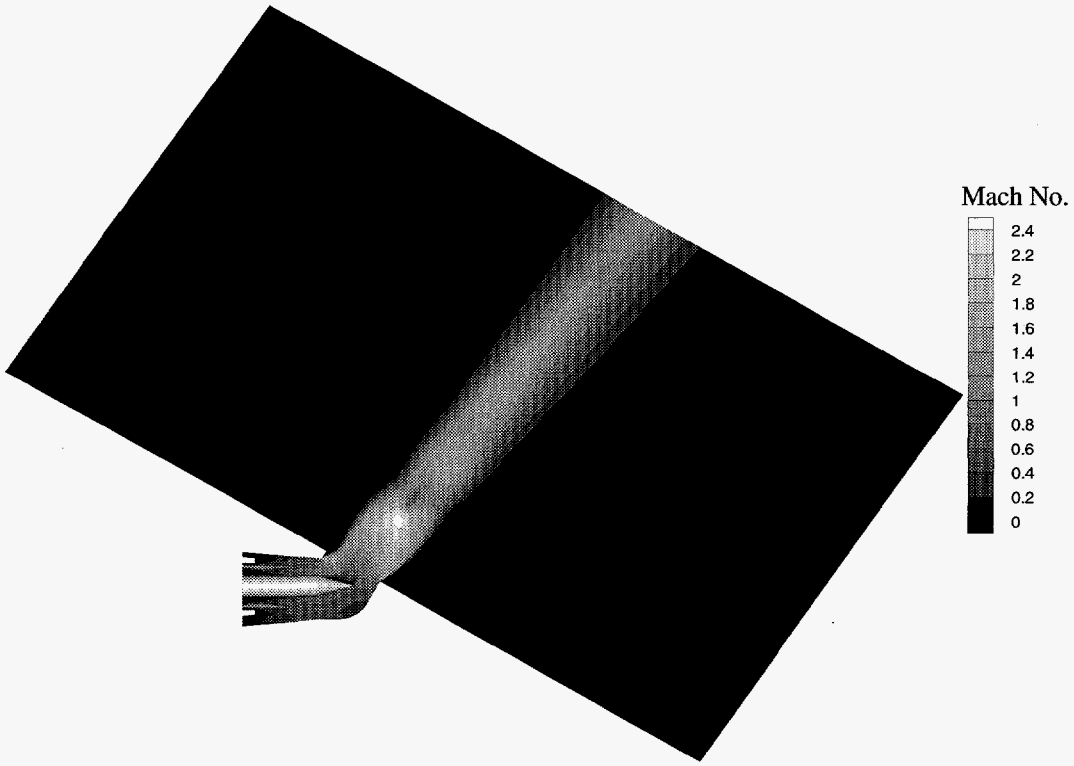

Figure 7. Gas Mach number contours in the plane of symmetry of the aircap and exterior.

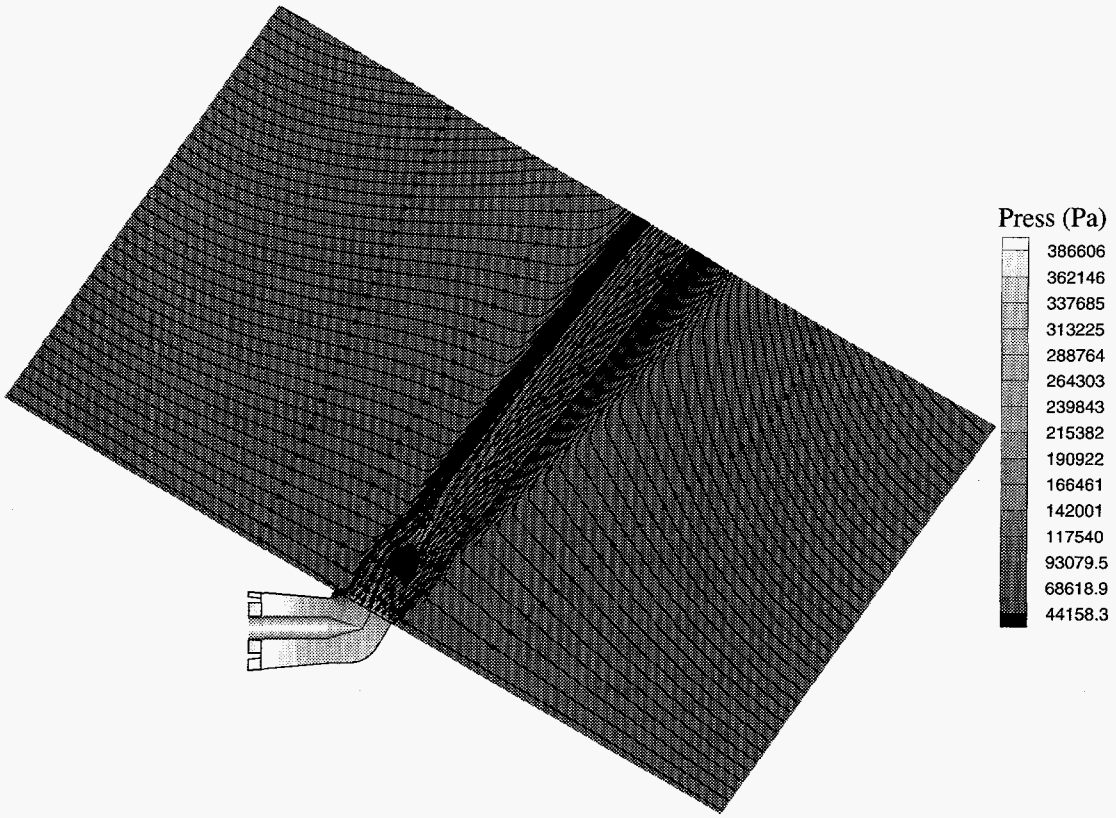

Figure 8. Streamline patterns in the plane of symmetry of the aircap and exterior.

ists on the upper portion of the aircap near the exit. The predicted spray angle of the torch is approximately 50 degrees; whereas, the geometric turn angle of the aircap is 60 degrees. This is an important difference, for example, in designing a curved aircap for a certain spray angle impinging on an engine cylinder bore. The streamlines also show the entrainment, or pumping, of ambient air from the upper and lower boundaries into the high speed jet. The peak velocity in the jet is about 2250 *m/sec* and decreases to a value of 1150 *m/sec* at the exit of the computational domain.

Figure 9 shows the gas temperature contours in the plane of symmetry. It can be seen that the gas temperature of the jet decreases as the flow convects downstream due to the turbulent entrainment of the ambient air. At the aircap exit, the peak gas temperature is approximately 3000 *K*. Then the temperature drops in the first expansion wave to about 2000 *K*. Next, the temperature rises in the first shock diamond to about 2250 *K*. Finally, the temperature decreases to about 1000 *K* at the exit of the computational domain. These high temperature jets of HVOF torches decay rapidly compared to cold gas jets due to their low density and the rapid entrainment of ambient air.

Particle Characteristics. Ten computational particles were injected into the gas flow field. Each of these computational particles represents a large number of actual steel particles in the stream, all with a diameter of 30 μm. The computational particles are evenly spaced along the leeside of the conical tip near the plane of symmetry. The injection points, which are on a line parallel to the conical tip, are displaced slightly normal to the surface to avoid being trapped in the separated flow region shown by the streamline pattern in Fig. 5.

Figure 10 shows the predicted trajectories of nine steel particles with respect to a coordinate system aligned with the axis of the nozzle. That is, the x coordinate is aligned with the centerline of the wire and y is normal to the wire. The centerline normal to the exit plane of the aircap is shown as a solid line in Fig. 10. Particle #1 was injected near the tip of the wire and Particle #10 was injected near the cylindrical portion of the wire, with the other 8 particles in between. As shown in Fig. 10, Particles #1-#5 remained closest to the exit centerline, while Particles #7-#10 fanned out away from the centerline. Particles #1-#5 were injected near the separated flow region, where the gas had dominant crossflow over the tip, and were immediately swept up by the gas flow towards the exit-plane centerline. Whereas, Particles #7-#10 were injected into a higher momentum gas flow primarily aligned with the wire which carried them over the separated flow region and further away from the exit centerline. Note that all particles were predicted to spray at angles less than the turn angle of the curved aircap. The trajectory for Particle #6 was almost identical to the trajectory of Particle #5 and was not included in Fig. 10.

Figure 11 shows the variations of the particle velocities with axial position. The position of the aircap exit is shown as a solid line in this figure. Ahead of the aircap exit, all par-

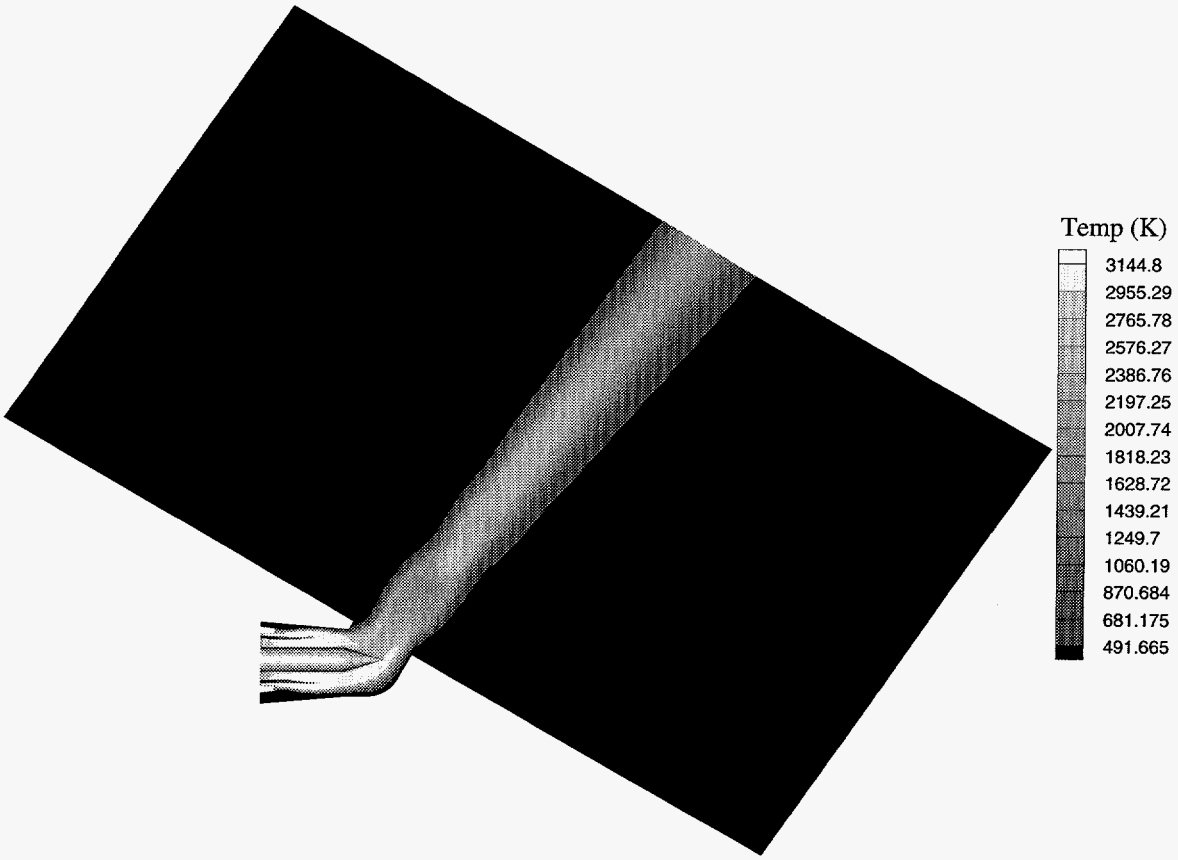

Figure 9. Gas temperature contours in the plane of symmetry of the aircap and exterior.

ticle velocities are inside the aircap. The particle velocities increase rapidly as the gas expands outside of the aircap. After a short distance, some of the velocities start to level off, for example, Particle #10. The reason for this is that their trajectory has taken them outside the high velocity spray jet into ambient air. At the end of the computational domain, Particle #2 has the largest velocity with a value of 310 *m/sec*.

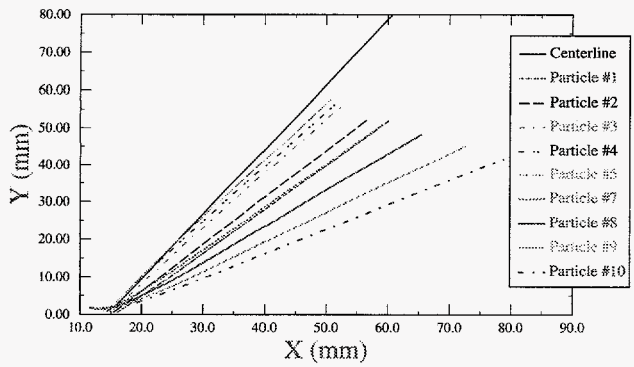

Figure 10. Predicted particle trajectories relative to the geometric centerline of the aircap exit.

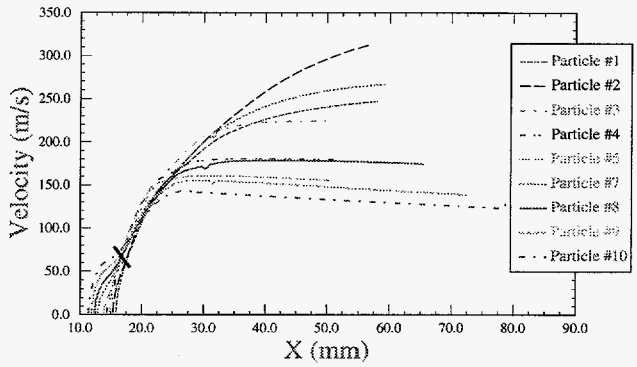

Figure 11. Predicted particle velocities from wire tip to edge of computational domain.

Figure 12 shows a contour plot of the velocity for all 10 particles outside of the aircap. The boundaries of the contour plot is based on the position of the particle trajectory curves. The maximum velocity region is located in the upper portion of the contour plot near the edge of the computational region. The line of peak particle velocities, at a given axial distance from the aircap exit, is seen to lie at an angle of 10 degrees from the geometric centerline of the aircap exit plane. The reason for this offset is that the peak jet velocities

are offset from the geometric centerline. The particle velocities outside of the aircap range between 100 *m/sec* to 310 *m/sec*.

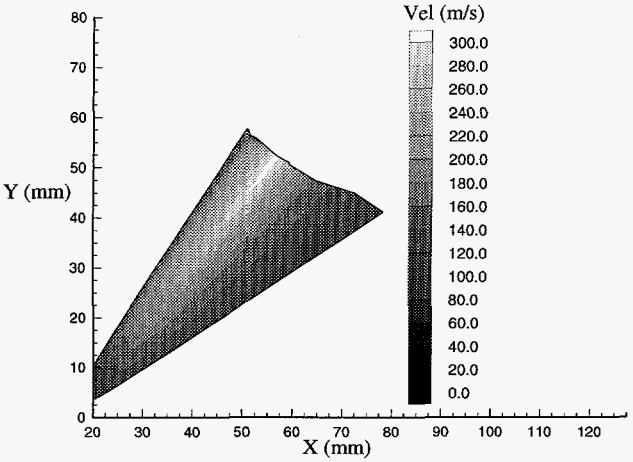

Figure 12. Particle velocity contours of numerical predictions.

Figure 13 shows a contour plot of the experimentally measured velocities. The 2-D grid overlaid on the velocity contours shows the locations at which the particle velocities were measured. The rectangular measurement region was intended to cover the region of maximum particle velocities, but it is seen that it did not quite capture the peak velocities. This is why the peak velocities are missing from the upper edge of the plot. This figure also shows zero velocity regions near the aircap exit and the lower edge of the experimental domain. Zero velocity measurements were the result of having too few particles in these regions to sample, not that the particle velocity is zero.

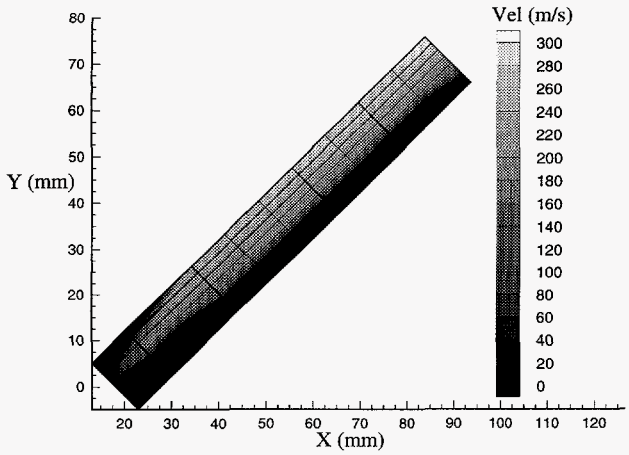

Figure 13. Particle velocity contours of experimental data.

Figure 14 shows particle velocity curves of both the numerical predictions and the experimental measurements. The experimental data curves are the velocity values along grid lines in the direction of flow. Only nonzero experimental data curves starting from the upper streamwise edge of Fig. 13 are shown in this figure. A sampling of the predicted velocity curves, including the maximum and minimum curves, are shown. It can be seen from this figure that the numerical results bound the experimental data and display the same trends with x. It should be noted that the numerical results are for individual particles that are tracked through the entire domain; whereas, in the experiment, velocities of many different particles are measured at each experimental grid point and the most frequently recorded value of velocity is computed. In other words, the band of velocities predicted in Fig. 14 is due to various paths, or trajectories, that the particles take. The path that a computational particle follows depends on the initial injection position. In the simulation, the particle injection positions were chosen to ensure that the particle trajectories spanned the region where velocity measurements were taken and so some of the computational particles did not necessarily simulate the initial position of the real metal droplets.

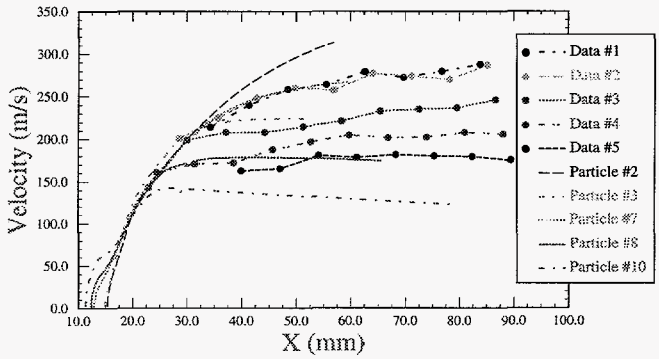

Figure 14. Particle velocities of both numerical predictions and experimental data.

Table 3 shows a direct comparison of the numerically predicted and experimentally measured particle velocities at three coincident locations. The three locations chosen are along Data #3 grid line which is in the middle of the experimental data. The predictions compare very well with the measured particle velocities up to about 40 *mm* from the inlet face.

Table 3. Measured and Predicted Particle Velocities

x (mm)	y (mm)	Measured V (m/sec)	Predicted V(m/sec)
22.5	9.3	143.1	147.3
30.0	16.4	198.9	192.6
37.1	23.5	208.0	218.1

Summary and Conclusions

Numerical and experimental results were presented for a HVOF spray device similar to a Metco DJRW torch. Computational results were presented for the internal combusting flow, the external jet decay, and the wire droplet flow field. Gas temperature, Mach number distributions, streamline patterns, and particle trajectories and velocities were discussed

to illustrate features of the complex three-dimensional flow. The peak temperature in the combustor was 3330 *K*, and the peak Mach number in the jet was 2.5. Laser Two-Focus (L2F) measurements were made to determine the wire sprayed particle velocities in the external plume. Very good agreement was obtained between the computational particles and the particle velocity measurements.

Future work should include additional validation of the numerical simulations. Experimental measurements of gas velocity, possibly using the L2F technique and submicron particle injection, and gas temperature should be made. With additional validation of several CFD predicted parameters, increasing confidence will be built in these type simulations. Although 3-D CFD simulations are complex and very computer intensive, they provide an unparalleled level of physical information concerning these devices. With this level of analysis, these numerical tools can be used to significantly improve and optimize HVOF spray torch designs.

Acknowledgements

The authors wish to thank Fritz Owens and Milind Talpallikar of CFD Research Corporation and Ron Dykhuizen of Sandia National Laboratories for their continued assistance and consultation on the two-phase flow. Also the authors wish to thank Mark Smith of the Sandia National Laboratories for his assistance with the experimental measurements.

This work was supported under United States Department of Energy, Cooperative Research and Development Agreement No. SC92-01104. This research was conducted jointly with the Powertrain Group of General Motors Corporation.

References

[1] Power, G. D., Barber, T. J., and Chiappetta, L. M., "Analysis of High Velocity Oxygen Fuel (HVOF) Thermal Torch," AIAA Paper No. 92-3598, July 1992.

[2] Power, G. D., Smith, E. B., Barber, T. J., and Chiappetta, L. M., "Analysis of a Combustion (HVOF) Spray Deposition Gun," UTRC Report 91-8, East Hartford, CT, March 1991.

[3] Smith, E. B., Power, G. D., Barber, T. J., and Chiappetta, L. M., "Application of Computational Fluid Dynamics to the HVOF Thermal Spray Gun," Proceedings of the International Thermal Spray Conference, Orlando, FL, May 1992, pp. 805-810.

[4] Oberkampf, W. L., and Talpallikar, M., "Analysis of a High-Velocity Oxygen-Fuel (HVOF) Thermal Spray Torch, Part 1: Numerical Formulation," Proceedings of the 7th National Thermal Spray Conference, Boston, MA, June 1994, pp. 381-386.

[5] Oberkampf, W. L., and Talpallikar, M., "Analysis of a High-Velocity Oxygen-Fuel (HVOF) Thermal Spray Torch, Part 2: Computational Results," Proceedings of the 7th National Thermal Spray Conference, Boston, MA, June 1994, pp. 387-392.

[6] Hassan, B., Oberkampf, W. L., Neiser, R. A., and Roemer, T. J., "Computational Fluid Dynamic Analysis of a High-Velocity Oxygen-Fuel (HVOF) Thermal Spray Torch," Presented at the 8th National Thermal Spray Conference, Houston, TX, September 1995.

[7] Hassan, B., Lopez, A. R., and Oberkampf, W. L., "Computational Analysis of a Three-Dimensional High-Velocity Oxygen-Fuel (HVOF) Thermal Spray Torch," Proceedings of the 8th National Thermal Spray Conference, Houston, TX, September 1995, pp. 193-198.

[8] Lai, Y. G., Przekwas, A. J., and So, R. M. C., "Aerodynamic Flow Simulation Using a Pressure-Based Method and a Two-Equation Turbulence Model," AIAA Paper No. 93-2902, July 1993.

[9] Jiang, Y., Lai, Y. G., Ho, S. Y., and Przekwas, A. J., "3D Simulations of Complex Flows with an Implicit Multi-Domain Approach," AIAA Paper No. 93-3124, July 1993.

[10] Launder, B. E., and Spaulding, D. B., "The Numerical Calculation of Turbulent Flows," *Computational Methods Applied to Mechanics and Engineering*, Vol. 3, 1974, pp. 269-289.

[11] Sarkar, S., "The Analysis and Modeling of Dilatational Terms in Compressible Turbulence," *Journal of Fluid Mechanics*, Vol. 227, 1991, pp. 473-493.

[12] Gordon, S., and McBride, B. J., "Computer Program for Calculation of Complex Chemical Equilibrium Compositions, Rocket Performance, Incident and Reflected Shocks, and Chapman-Jouguet Detonations," NASA SP-273, Interim Revision, March 1976 (New Version 1989).

[13] Westbrook, C. K., and Dryer, F. L., "Simplified Reaction Mechanisms for the Oxidation of Hydrocarbon Fuels in Flames," *Combustion of Science and Technology*, Vol. 27, 1981, pp. 31-43.

[14] Crowe, C. T., Sharma, M. P., and Stock, D. E., "The Particle-Source-In CELL (PSI-CELL) Model for Gas-Droplet Flows," *J. of Fluids Engineering*, 1977, pp. 325-332.

[15] GRIDGEN User's Manual, Version 10, Pointwise, Inc., Bedford, TX, March 1995.

[16] Smith, M. F., O'Hern, T. J., Brockmann, J. E., and Neiser, R. A., "A Comparison of Two Laser-Based Diagnostics for Analysis of Particles in Thermal Spray Streams," Proceedings of the 8th National Thermal Spray Conference, Houston, TX, September 1995, pp. 105-110.

[17] Neiser, R. A., Brockmann, J. E., O'Hern, T. J., Dykhuizen, R. C., and Smith, M. F., "Wire Melting And Droplet Atomization in a HVOF Jet," Proceedings of the 8th National Thermal Spray Conference, Houston, TX, September 1995, pp. 99-104.